Current Progress of the New Sub-millimeter Survey Instrument at JCMT: An Upgrade to SCUBA-2/POL-2 with 7272 MKIDs Detectors at 850 μm

Shaoliang Li[a], Dan Bintley[a], Paul T.P. Ho[a], Zheng Lou[b], Richard C.Y. Chou[c], Ray S. Furura[d], Nagayoshi Ohashi[a], Simon Doyle[e], Huabai Li[f], Junkun Huang[f], Janik Karoly[g,m], Kuan-Yu Liu[a], Dan Sinwong[h], Tai Oshima[i], Nario Kuno[j], Shunsuke Honda[j], Hiroyuki Nakanishi[k], Sarah Graves[a], Jamie Cookson[a], Mingtang Chen[c], Ran Duan[l], Derek Ward-Thompson[g], Steve Eales[e], Peter Barry[e], Shiling Yu[l], Mingzhu Zhang[l], Weitao Lyu[f], Wiphu Rujopakarn[h], Zhenhui Lin[b], Shengcai Shi[b]
[a]East Asian Observatory [b]Purple Mountain Observatory, CAS [c]Academia Sinica, Institute of Astronomy and Astrophysics [d]Tokushima University [e]Cardiff University [f]The Chinese University of Hong Kong [g]University of Central Lancashire [h]National Astronomical Research Institute of Thailand [i]National Astronomical Observatory of Japan [j]University of Tsukuba [k]Kagoshima University [l]National Astronomical Observatory of China [m]University College London

ABSTRACT

SCUBA-2[1]/POL-2[2] has been the most productive instrument at JCMT since it's fully commissioned[3] in 2011 September, and it's constantly oversubscribed during the call-for-proposals by a factor of 3 to 5. The proposed new 850μm instrument will feature 7272 state-of-the-art Microwave Kinetic Inductance Detectors (MKIDs)[4] operated below 100 mK, fully utilizing the JCMT's 12 arcmin Field of View (FoV), thus have all the capabilities of SCUBA-2 at 850 μm, yet will map an order of magnitude faster. The new instrument will be incorporated with intrinsic polarization measurement capability which is 3636 pixels. Mapping the 850 μm polarization will be improved by a factor of at least 20.

Keywords: SCUBA-2, JCMT, MKIDs, Superconducting Array, Polarimeter, Survey Instrument, Sub-millimeter

1. INTRODUCTION

SCUBA-2 was designed and built in the early 2000s and installed on the telescope in 2010. This very ambitious project has been a huge success and SCUBA-2 is still the premier submillimeter camera in the world. However, SCUBA-2 is a large and complex instrument designed to meet a wide range of science goals[1] and in every way pushed the existing technological capabilities in the field, all of which resulted in many compromises and complications. The new 850 μm instrument will have all of the capabilities of SCUBA-2 at 850 μm and yet will map an order of magnitude quicker. Large-scale structure in maps will be a better defined by virtue of a single uniform array and larger FoV. Mapping 850 μm polarization will be improved by a factor of at least 20. We will take advantage of huge steps forward in detector fabrication and performance. These will not only deliver the improved sensitivity and mapping speeds but simplify and speed up development, fabrication, integration and testing while dramatically reducing costs. In all other areas, including optics, cryogenics, and back-end data acquisition, the instrument will use well-tested technologies, while absorbing and adapting the lessons learned from the same team that built SCUBA and SCUBA-2.

In recent years, MKIDs detector arrays has advanced with their multiplexing readiness, comparing to the Transition Edge Sensor (TES) detector arrays that SCUBA-2 used. Easier fabrication and integration into the system also adds to the factor in choosing MKIDs over TES for the new instrument. After visiting NIST in 2018, we have planned the MKIDs detector array to be feed horn coupled[5] and polarization sensitive, 3636 detecting pixels in total. The design will be similar to those NIST have designed and fabricated for TolTEC[6], as shown in Figure 1.

With the feedback from the JCMT user community, it's decided that the new instrument will operate at 850 μm only. This is driven by the limited weather available at Mauna Kea for 450 μm, alongside the urgency of having an upgraded 850 μm survey instrument on sky.

Ground-based and Airborne Instrumentation for Astronomy X, edited by Julia J. Bryant, Kentaro Motohara, Joël R. D. Vernet, Proc. of SPIE Vol. 13096, 130967K
 · 0277-786X · doi: 10.1117/12.3018648

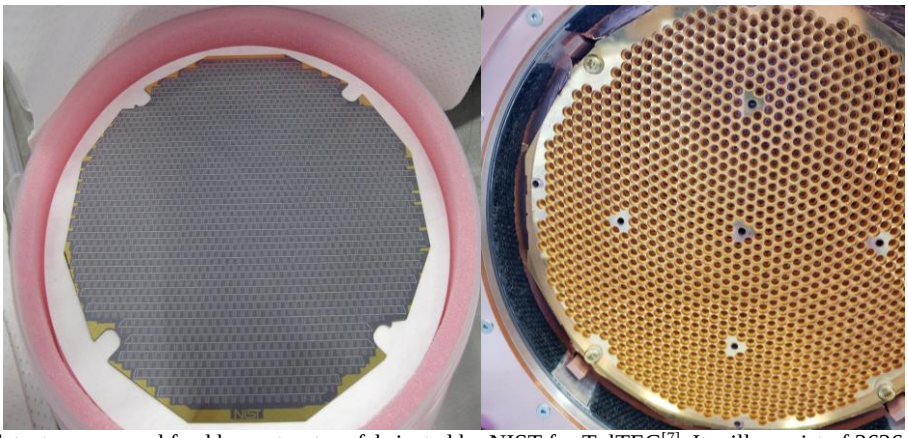

Figure 1. The detector array and feed horn structure fabricated by NIST for TolTEC[7]. It will consist of 3636 pixels at 1fλ spacing intervals, with 2 MKIDs detectors orthogonally polarized for each pixel. The incidental light will be feed horn coupled, reducing the stray light which has been a problem for SCUBA-2.

A comparison of the mapping speed improvement is listed in Table 1. The table also listed possible improvement for SCUBA-2 if the 12 arcmin circular FoV was fully utilized in the 2nd row, and if more sensitive detector arrays could be used to replace the current TES arrays in the 3rd row.

Table 1. Relative mapping speeds comparing the new MKIDs array to SCUBA-2 at 850 μm.

Instrument	FCF Jy/Pw	NEFD mJy $Hz^{1/2}$	FoV $arcmin^2$	Effective number of detectors	Relative Mapping speed
SCUBA-2	538	102	36	3072	1
SCUBA-2 (12' FoV fλ/2)	538	102	113	11921	4
SCUBA-2 (12' FoV fλ/2)	399	33	113	11921	38
New MKIDs (12' FoV 1fλ)	369	33	113	3636	10

The 10 times mapping speed improvement can be achieved with the following improvements:

1) Improved NEFD. When operating at photon noise limit, a factor of 2 improvement in NEFD would give a factor of 4 in mapping speed per pixel. To achieve the factor of 2 improvement, we'll tackle the following issues identified in SCUBA-2:
   - The excess detector noise and optical power. The excess detector noise can be identified with the measured weighted mean dark NEP, shown in Table 1 of [8]. While for the optical power, the stray light has been an issue for SCUBA-2 that cannot be effectively removed[9].
   - Comparing to the filled focal-plane SCUBA-2 array, the planned feedhorn-couple array for the new instrument would control the in-band stray light better[5], in addition to the electromagnetic interference that are better shielded.
   - By following the path of MUSCAT[14] and TolTEC[11] system design, which has detailed stray light control considerations, the excessive optical power can be controlled better.
   - Due to the intrinsic thermal conductivity of the plastic-based filters used on SCUBA-2, the emissivity or self-heating of the filters cannot be avoided. Benefiting from the newly designed Cardiff filters, the excessive optical power can be further suppressed.
2) The circular 12 arcmin FoV sampled at fλ, comparing to the effective SCUBA-2 6 arcmin square FoV, will give an increase of 3.
3) The feedhorn coupled detector array compared to the fλ/2 closed packed SCUBA-2 array would actually lower the number of pixels by a factor of 0.7.

4) For the yield of the detector array fabrication, we have assumed 80% as MUSCAT. The usable SCUBA-2 array pixels during a science observation is 60%. This would give an increase of 1.3. If the trimming technology could be applied, this would be 1.7 instead.

2. POWER LOADING MODELING

2.1 Power loading model overview

The goal of the new detector as mentioned before is to increase the FoV and the mapping speed over the previous SCUBA-2 detector. Increasing the FoV is dependent on the focal plane array, optics and size of detector. To determine the increase of mapping speed, an accurate estimation of the Noise Equivalent Flux Density (NEFD) is required. The NEFD is the flux density that produces a Signal-to-Noise Ratio (SNR) of one in one second of integration time. It is a measure of the sensitivity on the sky where a smaller NEFD is more desirable. The Noise Equivalent Power (NEP) quantifies a photodetector's sensitivity or the power generated by a noise source. The signal power is such that it gives a SNR of one in one Hz output bandwidth. A value of 10^{-12} W·Hz$^{-1/2}$ means a detector can detect a signal power of 1pW with a SNR of one after 0.5 seconds of averaging.

An accurate estimate of the optical load on the detector requires a model of the entire set up of the instrument. We have set up two models for testing the optical loading. One is using a template from the previous instrument, SCUBA-2, modeling the transmission and power of each component along the light path. This includes all of the ambient optics and all of the components in the cryogen. These parameters have not yet been decided for the current proposed instrument, where the optical components and their associated temperatures are not certain. This makes using this model at the moment difficult, but we outline its methodology below and adopt values from SCUBA-2. The second model is using the open-source Python codes from Bryan et al. (2018)[10] which were developed for the purpose of calculating the power loading and mapping speed of the TolTEC instrument[11] on the Large Millimeter Telescope (LMT). In the future, we will attempt to also use the BoloCalc model code from the Simons Observatory[12].

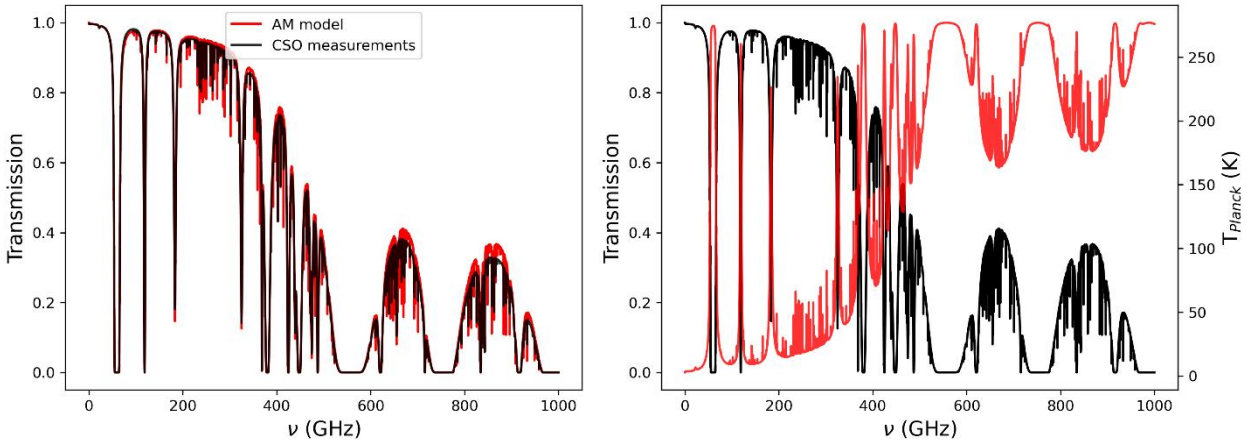

Figure 2. Left: A comparison of the archival CSO transmission observations and the transmission predictions of the *am*[13] models at Band 2 weather conditions (t=0.05, Precipitable Water Vapor PWV=0.83). These observations are at zenith. Transmission will vary with altitude. Right: A plot of the transmission from the *am* models plotted with the Planck Brightness Temperature which is used for the sky temperature in the TolTEC model. This was also calculated for Band 2 weather conditions.

The sky is the dominant source of incident power on the telescope, something which is also seen in MUSCAT on the LMT[14], though it operates at a different frequency and different site. While this emission will be both filtered out within the optical path and eventually removed in data reduction processes, the amount of sky power that is incident on the detector must be well-understood. To do this we must have a reliable model of the atmosphere at Mauna Kea. There is both historical atmospheric data from JCMT and CSO and the ability to model the atmosphere using *am*. *am* provides data-driven models of atmospheric emission and transmission and includes atmospheric profiles for Mauna Kea from archived weather satellite data as a part of the MERRA project run by NASA. A comparison between these models and

the archival CSO weather data can be seen in Figure 2 where the model agrees well with the measured data. We can run these models for a variety of weather conditions and altitudes. The models output atmospheric transmission as well as atmospheric temperature. The SCUBA-2 model makes use of the transmission data while the TolTEC model makes use of the atmospheric temperature as outlined below.

There are many factors which influence the calculations below. The bandwidth and central frequency of the detector will determine how much background power is received, both from the sky and all components along the optical path. The efficiency of the cold stop, the window, the filters and the eventual internal and external optics will all play a role in this calculation as well. However, the power contribution of these components is significantly less than the primary /secondary mirrors and the sky, both of which are then controlled by choice of central frequency and bandwidth. In the SCUBA-2 model, the sky and primary mirror contributed nearly 85% of the total background power.

We've assumed a similar cryogenic design to SCUBA-2[1]. This consists of the window and then a stray light blocker, at 280 and 150 Kelvin respectively. Then for the out-of-cabin, it would go lens (50 K), cold stop (50 K), lens (4 K) and for the in-cabin design it will be cold stop (50 K) then lens (4 K). Then after those optics, we assume there will be the edge filters, a bandpass filter, and an additional blocker all before the detector. Those additional components will be at 4 K while the detector will be at 100 mK. For the ambient mirrors, the in-cabin design has just one while the out-of-cabin design makes use of the existing C1-3 mirrors and then two additional mirrors.

2.2 SCUBA-2 model

The original SCUBA-2 model was developed for the TES detector without feed horns that eventually became SCUBA-2. There was a second model developed which included the use of feed horns which we use here. We will have to adjust certain calculations for the new MKIDs as well as the new array size, in terms of both physical size and number of pixels.

This model uses input atmospheric transmission values and calculates then the transmission at a given air mass level (to account for varied altitude) and then uses this adjusted transmission to calculate the emitted power of the atmosphere, integrating across the entire frequency range (although accounting for the bandpass filter) to get the background sky power in pW. This is the dominant source of background power, up to and sometimes exceeding 50% and the second highest contribution comes from the primary and secondary mirrors, with the total contribution from those two factors being up to 85%.

Then the net transmission at each point along the optical path is calculated. The background power is also calculated for each component along the optical path, including the primary, secondary and tertiary mirrors, then the optics feeding the light to the instrument as a single system, and then all the components within the instrument such as the window, additional optics (mirrors and lenses), filters and the detector. In addition, the emissivity (one minus transmission), the photon noise and the net transmission are all calculated. Then the total background power and photon noise is calculated by adding up the values of all the components. The minimum photon NEP is taken to be the sum of the photon noises. The total NEP is then adding in quadrature the photon NEP and the detector NEP. The detector NEP is taken to be a ratio of the minimum photon NEP where we take the ratio to be 0.5.

Without the complete design of the interior filters, we adopt the values from the SCUBA-2 cryostat. We remove the dichroic filter and the additional optical elements that SCUBA-2 has (see [1] for the complete design). For the in-cabin design, we keep the blocker (cold stop), one optics element (the silicon lens) and then the edge filters, bandpass, blockers and finally the detector. For the out-of-cabin design, we use the same as in-cabin but add in the additional 2 optical components, the High Density Polyethylene (HDPE) window and the second lens (in addition to the cold stop and first lens). We treat all ambient mirrors as having a tolerance/roughness of 2 micron and the roughness of the primary being 20 micron. The Ruze scattering factor is calculated for all of the mirrors which is accounted for in their transmission calculations.

The NEFD of SCUBA-2 was originally measured to be approximately 90 $mJy \cdot s^{1/2}$ in good observing conditions, though this was a factor of 2 worse than predicted[1]. We run our modeling for JCMT weather bands 1-4, where weather band 1 is τ=0.04, weather band 2 is τ =0.05 and weather band 3 is τ =0.08 and weather band 4 is τ =0.12. For these four weather band windows, we get NEFD values of approximately 16 $mJy \cdot s^{1/2}$, 18 $mJy \cdot s^{1/2}$, 23.5 $mJy \cdot s^{1/2}$ and 31.5 $mJy \cdot s^{1/2}$ respectively. For all calculations, the in-cabin and out-of-cabin designs give similar values. However, this may be due to the feed optics being treated as a singular component whereas in reality, the in-cabin design will only have one additional ambient mirror whereas the out-of-cabin design will have five. The NEP values are 1.2, 1.3, 1.4 and 1.5×10^{-16}

$W \cdot Hz^{-1/2}$ respectively and the background power values are 19.8, 22.6, 28.7 and 35.4 pW respectively. These were all calculated using a central frequency of 352.697 GHz, a bandpass of 35 GHz and an air mass of 1. Figure 3 shows how the power and photon noise vary for each component, dependent on the bandpass. The relative contribution of each component is similar across the different weather bands, so we just use Band 2 data to demonstrate this.

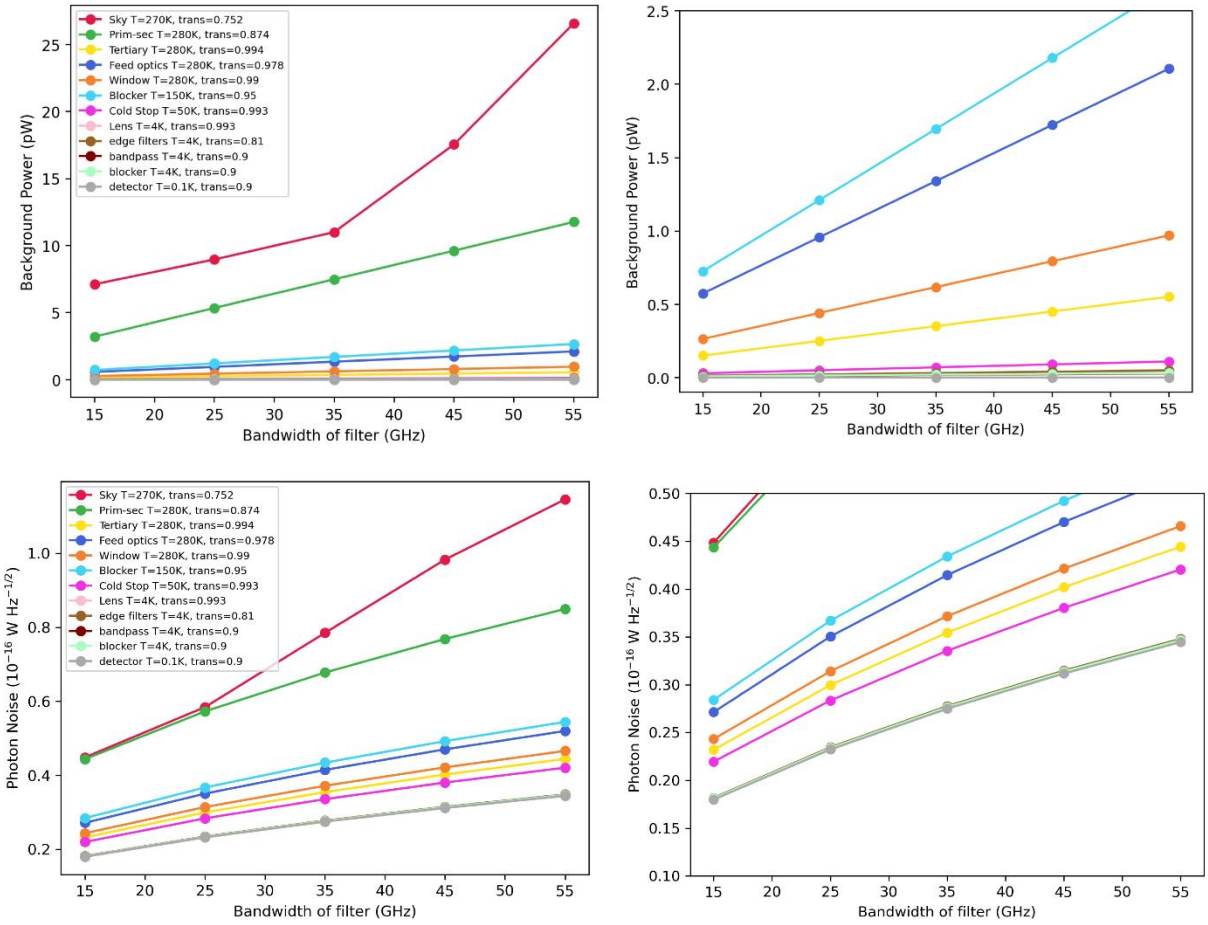

Figure 3. The relative power loading (upper) and photon noise (lower) contribution of the different elements in the design. Details about each are given in the text. The right column is a zoom in on the left plots to better illustrate the contribution of the other components.

Overall, the values we calculate using this model are reasonable and comparable order of magnitude to SCUBA-2. No comparisons have been made here with mapping speed. However, the increased number of detectors that we will have with the MKIDs will further increase the mapping speed (see 2.3 TolTEC model section), so we should be on the order of at least a few times increase in mapping speed. But we are aware of the higher SCUBA-2 NEFD values that were measured[1]. This may be a factor that we want to then consider. We also show here how the NEFD and background power vary with sky transmission. This can be seen in Figure 4. The *am* models are still used to give transmission values, but we vary the air mass from 1 to 15 in the SCUBA-2 model to give different values of sky transmission. This is equivalent to varying the degree of observation, to account for altitudes of different sources in a night of observing. To compare these values, measured NEFD values of SCUBA-2 are shown in the lower right plot of Figure 4. We can see that in general, in our better weather conditions, we model lower NEFD values.

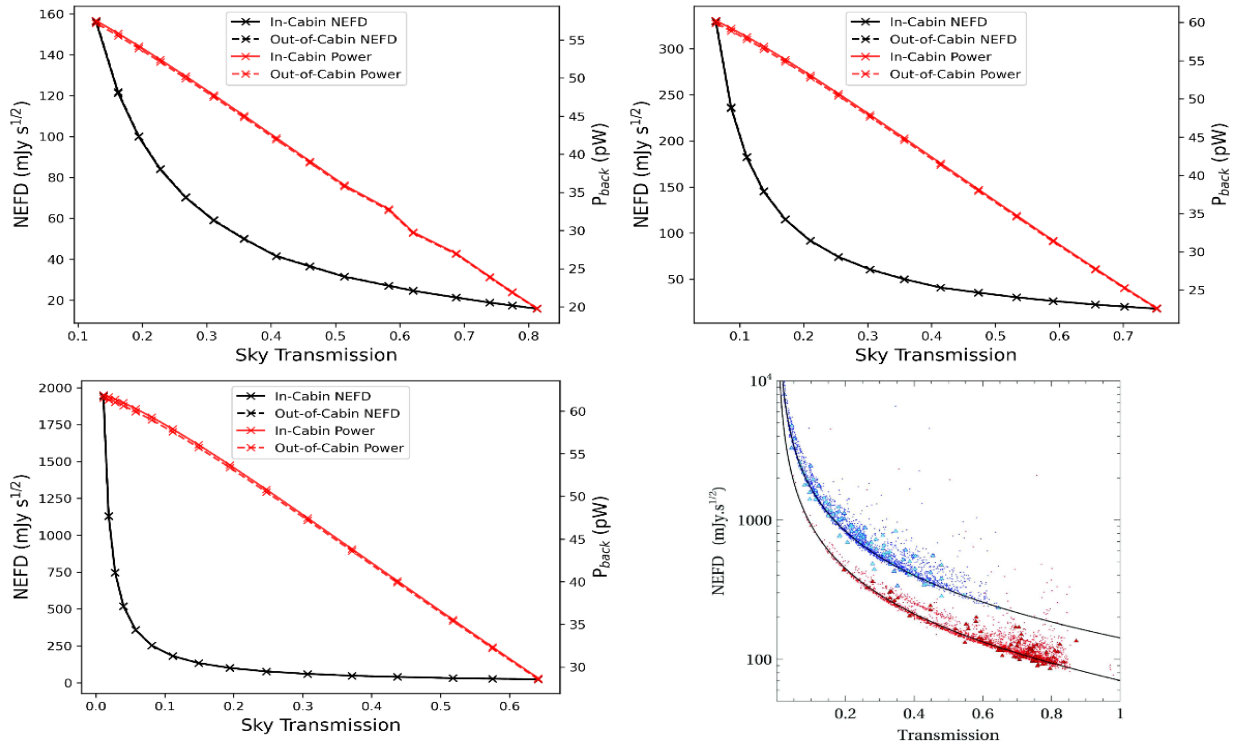

Figure 4. Variation of background power and the NEFD from the SCUBA-2 model based on different sky transmission values. All values come from *am* models run with PWV=0.58 (Band 1, upper left), PWV=0.83 (Band 2, upper right) and PWV=1.58 (Band 3, lower left). We then vary air mass from 1 to 15 to account for different observing angles. Both in-cabin and out-of-cabin values are plotted, but they are very similar. The lower right plot has been taken from Figure 13 of [1] to compare measured SCUBA-2 NEFD values.

2.3 TolTEC model

For a complete description of this method, see [11]. Here we will give a short summary of the method as well as our calculated results.

We use the *am* models to estimate the sky temperature. This can be seen in the right plot of Figure 2. This is the base emission temperature for the model. We add to this the temperature of the primary, secondary and tertiary mirrors, scaling 280 K by their emission (taken from the SCUBA-2 model, approximately 0.13) and the temperature of the other mirrors. For the other mirrors, we use five mirrors at 280 K with 0.02 emission for the out-of-cabin design and then one mirror at 280 K with 0.02 emission for the in-cabin. Finally, that temperature is scaled by the instrument efficiency to determine an at-detector temperature. Here we do not yet know the instrument efficiency which includes aperture efficiency, filters, feed horn and detector optical efficiency factors. As can be seen in Figure 5, we therefore run this model for a variety of aperture and detector optical efficiencies, but we do not consider efficiency of the feed horns. We do apply a passband filter to the data. This passband filter is the same one used in SCUBA-2 though this will most likely change for this new instrument. We also do not explicitly consider the internal lenses which are currently a part of the design. These will need to be modeled once we know what edge filters, exact bandpass and other filters we will be using.

The temperature, which now considers components along the optical path and approximations for the instrument, is then converted to a power value assuming the loading has a Rayleigh-Jean spectrum. It is calculated for a single-polarization detector. This calculated power and still the at-detector temperature is used to calculate the shot noise (from loading) and wave noise (from single polarization). The shot and wave noise are added in quadrature to get the total at-detector NEP. This NEP is then further scaled by a factor which takes into account the internal noise level of the detector contributing to the NEP.

Then the NEP, which is currently the at-detector value, is scaled to then become the on-sky NEP. The at-detector NEP is divided by the system efficiency and by the atmospheric transmission which gives then the on-sky sensitivity of a single-detector with its single-polarization sensitivity[11]. The NEFD is then calculated as

$$NEFD = NEP \frac{2 \times 10^{26}}{\sqrt{2\pi \left(\frac{D}{2}\right)^2 df}}$$

where D is the diameter of the JCMT dish and df is the step factor of frequencies, where the final NEFD is then the weighted sum of the NEFD values at each frequency step (see Eq. 9 of [11]). The total NEP is then the sum of squares across all the frequency steps. The total power loading, total NEP value and total NEFD are plotted in Figure 5 for a variety of aperture and detector efficiencies.

The TolTEC model defines mapping speed as the number of square degrees of sky that can be mapped to a 1 mJy noise level in beam-sized map pixels in an hour, hence giving mapping speed in units of square degrees per mJy^2 per hour[11]. The mapping speed is calculated as

$$MappingSpeed = \frac{3600 \times N_{det}}{N_{beams} \times NEFD^2} deg^2/mJy^2/hour$$

where N_{det} is the number of detectors (here 3636 MKIDs), N_{beams} is the number of beams in a square degree, given as

$$N_{beams} = \frac{(60 \times 60)^2}{FWHM^2 \times \pi/(4ln2)}$$

where FWHM is in arcseconds[11]. This shows that the mapping speed would scale by $N_{det}/NEFD^2$. The plan of 3636 MKIDs pixels is approximately the same number of detectors as SCUBA-2 for the continuum detection (for polarization it would be doubled), especially when considering the number of SCUBA-2 detectors that are not online[1]. Lower NEFD values are then also squared to further increase the mapping speed.

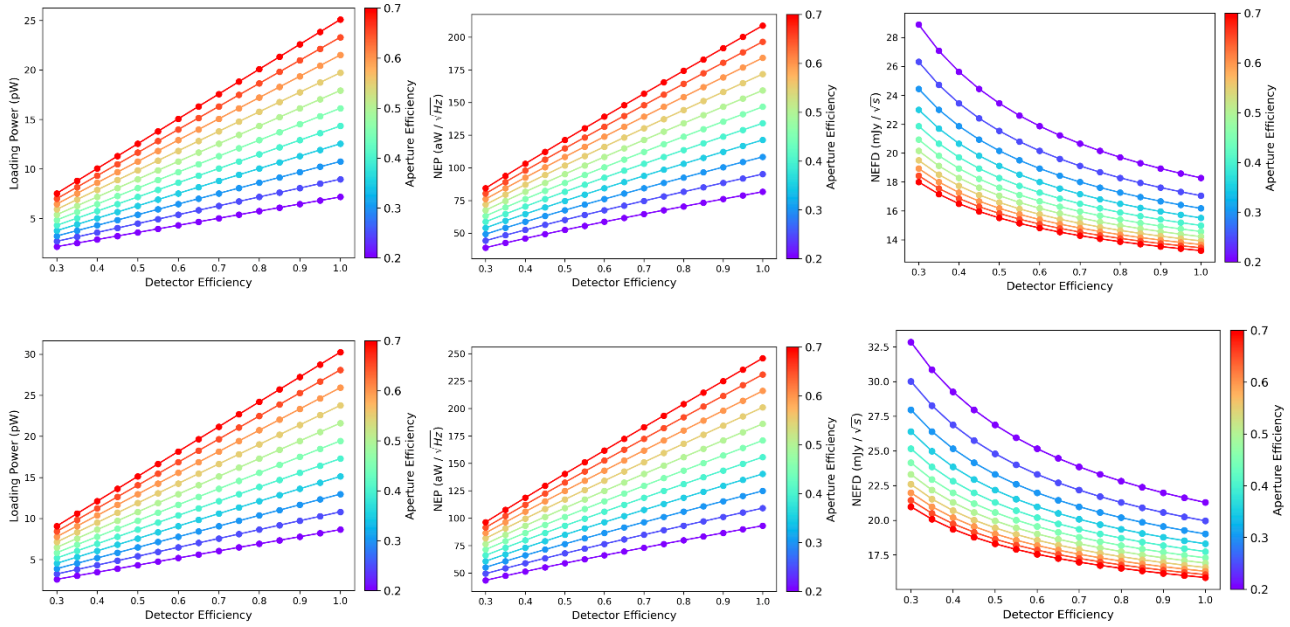

Figure 5. Upper row: The loading power, NEP and NEFD for the in-cabin design. Lower row: The same as the upper row but for the out-of-cabin design. See text for details of the model. These plots show the power, NEP (1 aW = 10^{-18} W) and NEFD values for a variety of detector and aperture efficiencies. All are calculated using Band 2 *am* models.

The TolTEC model uses an aperture efficiency of 0.35 which it states as being the aperture efficiency of 1 Fλ feed horns. We therefore adopt this value when calculating mapping speed. We also use a detector efficiency of 0.8 for the out-of-cabin and 0.85 for the in-cabin due to current modeling of the optical systems for those designs and their total efficiency.

We use the NEFD values calculated using these values. We also have only done these models for the zenith models. The *am* models can consider observing degree which will be similar to varying air mass as we did above. We calculate the mapping speed for the in-cabin design for the new instrument and then we calculate the mapping speed for both SCUBA-2 and the new instrument for the out-of-cabin design since the optical setup is similar to SCUBA-2. This gives us a basis to compare the values. The mapping speeds we calculate with these NEFD values presented here are slightly higher than SCUBA-2 but of similar order of magnitude. However neither of these models account for the FoV or the relative increase in the yield of the detector array fabrication, both of which are factors mentioned in Section 1 which would increase the mapping speed.

We obtain order of magnitude estimations of the NEP and NEFD for the in-cabin and out-of-cabin designs. This order of magnitude is similar to what was predicted for SCUBA-2. This is reasonable since we are dealing with the same site and hence same sky power that SCUBA-2 observes. Since the sky power is the dominant optical power load, we would expect a similar NEP and then NEFD. SCUBA-2 however had a higher measured NEFD by approximately a factor of 2. What we show is that the new designs would decrease the predicted NEFD (which was 45 mJy·s$^{1/2}$ for SCUBA-2[1]), but we are ultimately unable to properly model where this factor of 2 degradation came from, whether it be stray light or radiating optics. However, we can approximate how the choice of bandpass and central frequency will affect the optical power loading and the NEFD. In addition, we can estimate the emission from the various optical elements. Doing all of this provides an initial estimate of the NEP and NEFD we should aim for. However, the major improvement will be determining where the factor of 2 degradation in SCUBA-2's NEFD comes from. Being able to design a new optical system to limit that loss will ultimately give the increase in actual NEFD which will in turn increase the mapping speed.

2.4 Summary

Overall, we present initial estimates from our currently available models. There is not yet a settled design for the optics or cryogenics of the instrument, so proper modeling is not yet possible. We will also include BoloCalc models to compare against our values presented here. We do however find power loading and NEFD values which are of reasonable order of magnitude and do present a small increase in the predicted sensitivity over previous SCUBA-2 values. Together with the increase in number of detectors and the robustness of MKIDs, this indicates an increase in performance over SCUBA-2 of this new instrument. Values from the SCUBA-2 model do not show a remarkable difference between the in- and out-of-cabin design, but the TolTEC model does show some differences, on the order of a 3-5 mJy·s$^{1/2}$ for the NEFD and 3-5 pW for the power loading, with the in-cabin design providing the higher sensitivity. As discussed in Section 1, to determine an actual increase in performance over SCUBA-2, the identification and suppression of where the factor of 2 increase in NEFD came from for SCUBA-2 is key for increasing the mapping speed. What we can contribute with the models are ideal scenarios and order of magnitude estimates, as well as determining the effect of different sky parameters (PWV, airmass, etc) and optical design of the instrument in terms of bandwidth and central frequency.

3. POLARIMETER

The study of geometry of magnetic fields is essential for understanding the star formation processes and the physics of molecular clouds. The basic idea of polarization detection is to use a polarizer to extract the polarization information. Before being analyzed by the polarizer, the signal is usually modulated by a rotating half wave plate, thus in modulation periods, the amplitude and phase of the signal received by the detector can reveal the fraction and direction of polarization respectively.

However, the observation of polarization involves a major challenge resulted from the atmosphere, as the polarization fraction of dust emission is small, and water vapor is a good absorber and emitter at submillimeter wavelengths, so it introduces strong sky noise. The basic idea to overcome this challenge in polarimeters is to take difference between orthogonal polarizations in order to eliminate the unpolarized sky noise. Since the sky noise fluctuates with atmospheric conditions, two major strategies are adopted to ensure that the noise is stable when taking differences. The first strategy is to modulate the signal in a frequency higher than the sky noise fluctuations to make the noise stable in some modulation periods. The second strategy is to record the signal by different detectors simultaneously, ensuring that the sky noise can be effectively cancelled, thus the modulation frequency need not to be as high as in the first strategy.

Unlike SCUBA-2, the new instrument would have polarimetry capability built in: one pixel is composed of two MKIDs detectors at orthogonal polarization, as described above in the second strategy. In addition, we would also have the slow modulating Half Wave Plate (HWP) as POL-2[2] does. The HWP would also be located in front of the cryostat window.

Based on the optical design as discussed in the next session, there might be challenges if it's the in-cabin optics. For now, the polarimeter design is pending on the final decision on the optics.

4. OPTICAL DESIGN

4.1 Design requirements

The new optics is required to fill the whole field of view of 12 arcmin that's available at JCMT, operated at 850μm only. In addition to the FoV requirement, other requirements and inputs for the optical design include: 1) a cold stop is needed inside the cryostat for an efficient control of stray light. A fairly good pupil quality is required on the cold stop; 2) Since the new instrument will use feedhorn-type of detectors, focal-plane telecentricity is desired so that a planar detector array can be placed on the focal plane; 3) Final focal ratio is fixed to be F/2.5 to match the physical size of the detector array; 4) Strehl ratio as high as possible across the entire FoV is desired to maximize imaging quality and efficiency.

Two possible locations for the new instrument are either inside the Cassegrain cabin or out of the cabin on the Nasmyth platform. Optical designs are developed for both configurations and one of the most important purpose of this design study is to compare the advantages and disadvantages for the in-cabin and out-of-cabin designs in a comprehensive manner. We also deicide to consider a combination of mirrors and lenses to relay the telescope beams to the final focal plane, while purely reflective optics are used for SCUBA-2 and one of the out-of-cabin designs.

We have developed a total of six optical designs: one in-cabin and five out-of-cabin, with the following considerations:

- Maximum achievable field of view
- The space confinement
- The offline time for SCUBA-2
- Impact of the antenna tilting on the cryogenics and the polarimeter
- The modification to the current telescope structure needed
- The possibility of accommodating FTS-2

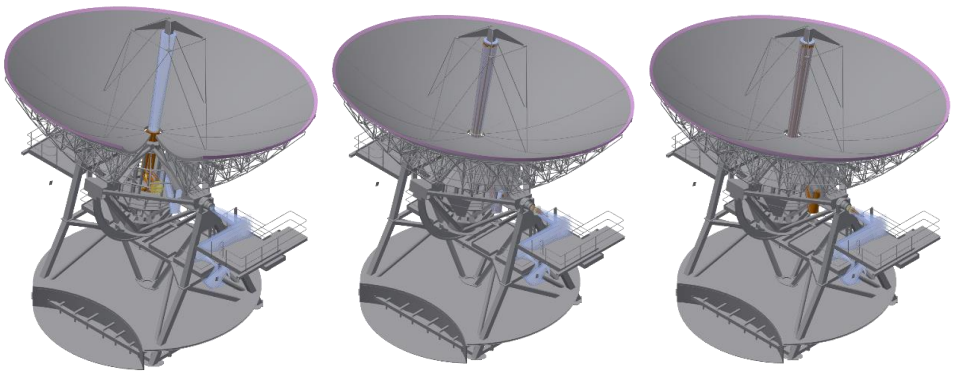

1 2 3

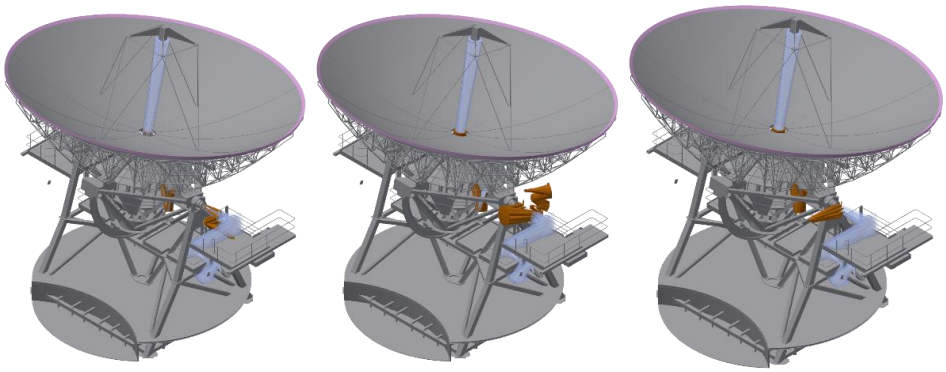

4 5 6

Figure 6. The optical designs (orange) with SCUBA-2 optics (light blue) as reference. Design 1 is the in-cabin design, aiming for a larger FoV and no interruption for SCUBA-2 observations. The difference between design 2 and 3 is the modification of the three mirrors before the bearing tube, thus the sizes of the lenses and windows have changes. Design 4 introduced two mirrors, further reducing the number and size of the lens and the window. Design 5 and 6 added a folding mirror after the bearing tube, so it could be used to reduce the interruption of SCUBA-2 observations. Design 5 uses all mirrors in order to achieve the maximum possible optical efficiency as SCUBA-2 did, while design 6 introduces lenses to minimize the space envelop.

4.2 In-cabin design

By placing the instrument right inside the Cassegrain cabin, a shorter optical chain can be designed for the relay optics, which helps to boost system transmission and ease the optical alignment process. The relay beams do not need to pass the long bearing tube so that an even larger FoV can be potentially realized. However, due to the beam obscuration by various mechanical structures inside the cabin, there is not much margin for further FoV enlargement. The optical layout for the in-cabin design I shown in Figure 6. The beams from the telescope is first reflected by a planar tertiary mirror and then converged by a curved fourth mirror which creates a pupil right behind the cryostat window. After passing the HDPE window, the beams pass through the cold stop and is finally brought into focus by a cold reimaging silicon lens, as shown in Figure 7. The lens also makes the final focus telecentric.

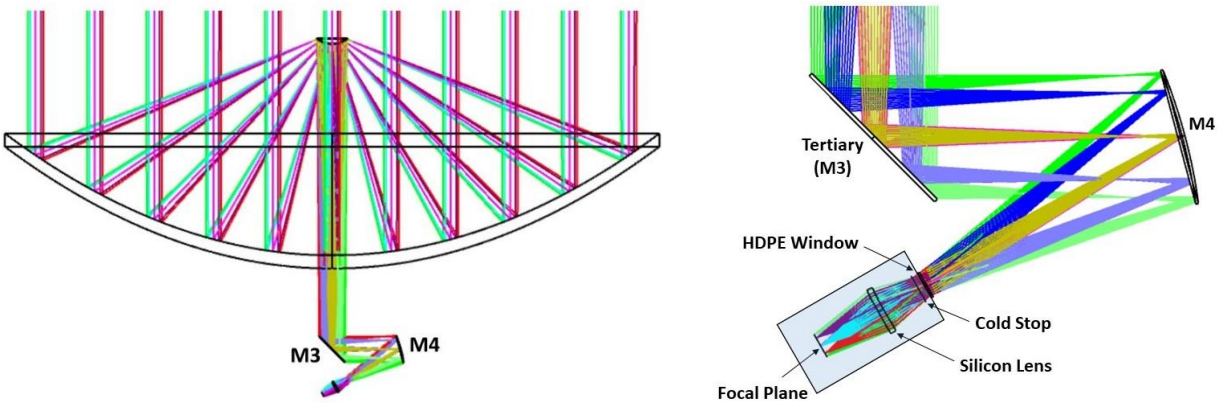

Figure 7. Optical layout for the in-cabin design (Design 1 in Figure 6). Left: Overall layout; right: zoomed in view of the Cassegrain cabin optics.

The fourth mirror is a freeform mirror with a diameter of 700 mm whose surface figure is described by polynomials. The cold lens is made of high-resistivity silicon and has a diameter of 250 mm. It has freeform surfaces on both sides. AR coating is needed on both lens surfaces due to the relatively high refractive index of silicon. The 140 mm cryostat window is made of HDPE which is almost transparent to submillimeter waves. The calculated Strehl ratio over the 12 arcmin FoV is shown in Figure 8. The Strehl ratio is relatively uniform across the FoV with an average of 0.975, showing diffraction-limited imaging quality can be delivered to the focal plane across the entire FoV.

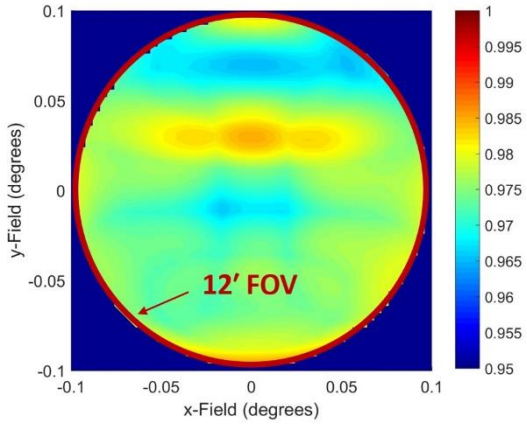

Figure 8. Strehl ratio map for the in-cabin design (Design 1 in Figure 6).

4.3 Out-of-cabin design

Moving the new instrument from Cassegrain cabin to Nasmyth platform provides several benefits such as easier design for the cryocoolers, compatibility to the insertion of a Fourier Transform Spectrometer (FTS) instrument, and better accessibility for maintenance. However, a longer optical chain is needed to relay the telescope beams to the Nasmyth instrument. The optical layout for the out-of-cabin design is shown in Figure 8. The tertiary and the following relay mirrors (C1, C2, and C3) are identical to those of the SCUBA-2. An intermediate F/7 focus is generated at the exit of the bearing tube. The clear aperture of the bearing tube is 390mm, which allows passing of a beam envelop of 12 arcmin diameter FoV. After the bearing tube, two additional ambient mirrors are used to further relay the beams to the cryostat. Inside the cryostat, a silicon lens is used to produce the final F/2.5 telecentric focus.

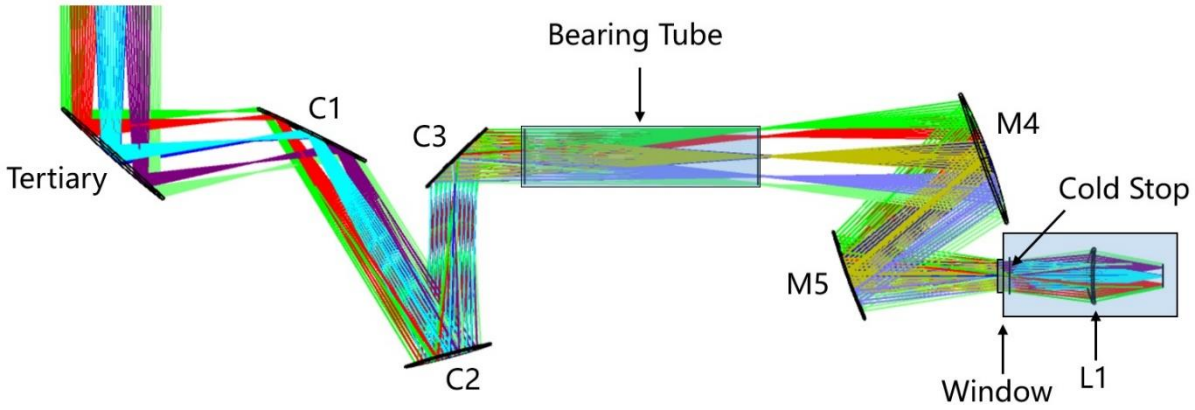

Figure 9. Optical layout for the out-of-cabin design (Design 4 in Figure 6). The primary and sub-reflector are not shown.

All the mirror and lens surfaces are freeform surfaces described by polynomials up to seven terms. The M4 and M5 mirrors have a diameter of 860 mm and 570 mm, respectively. The silicon lens has a meniscus shape and a diameter of 360 mm. The Strehl ratio is slightly lower than that of the in-cabin design, with an average of 0.96 across the FoV of 12 arcmin, as shown in Figure 10. We have also developed out-of-cabin designs with cryostat window directly facing the exit of the bearing tube and with two lenses in the cold optics. However, the two-lens systems (Design 2 and 3 in Figure 6) turn out to produce more loss than the design in Figure 9. This is clearly shown in Table 2 in the next section 4.4 Design comparisons.

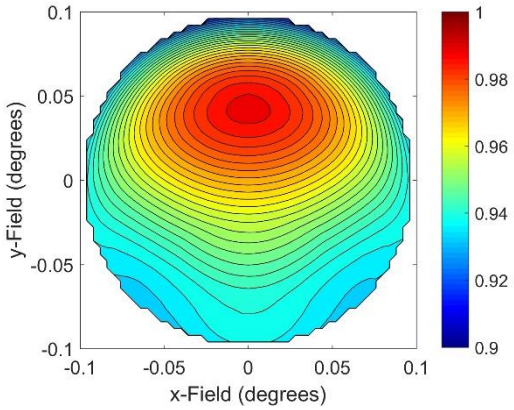

Figure 10. Strehl ratio map for the out-of-cabin design (Design 4 in Figure 6).

Other than the above mentioned design, we also developed another two, aiming to commission the instrument without interrupting the normal operation of SCUBA-2. However, this also adds to the complexity of the designs, as the optical path is occupied by SCUBA-2. To resolve this, a folding mirror is introduced right after the bearing tube on the Nasmyth platform, so the optical path could be directed sideways. There are two designs, one is the full reflective mirror design and the other one is a mixture of a fold mirror plus lenses design. Both designs can achieve a FoV of 12 × 12 arcmin.

The full reflective design contains 10 mirrors, excluding the tertiary mirror. Among the 10 mirrors, three of them locate in the telescope cabin (C1 – C3 in Figure 11 top panel) and seven mirrors (CM1 – CM6 plus the fold mirror) locate outside the telescope cabin. Figure 11 shows the optical layout of the full reflective design.

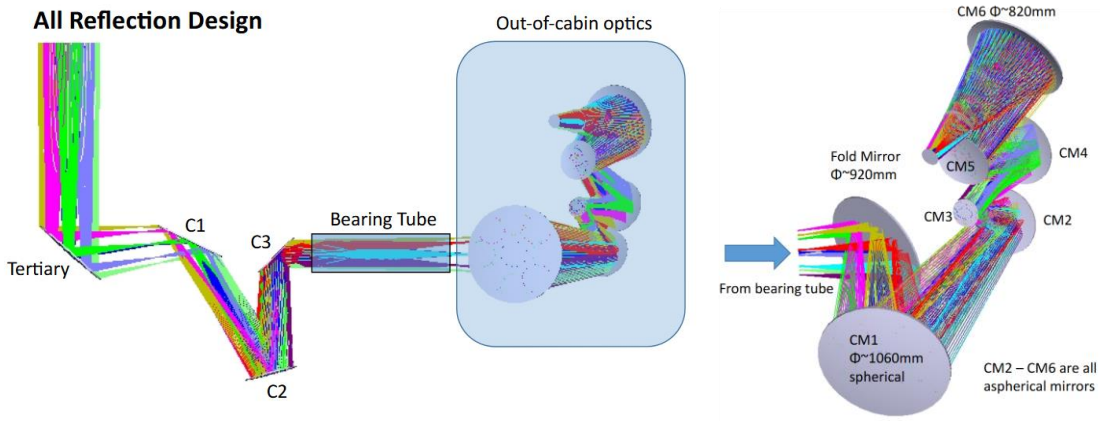

Figure 11. Left side shows the optical layout of the all reflective out-cabin design (Design 5 in Figure 6), the right panel is the zoomed in view of the out-of-cabin parts.

There are two spherical mirrors, which are the fold mirror and the CM1 mirror in the out-cabin part. These mirrors have a diameter more than 900mm and is too difficult to produce as aspherical surfaces. Other than that, the rest mirrors are aspherical ones described by polynomials. The out-of-cabin envelope is roughly 2500 mm × 2100mm × 1600 mm. The optical performance of the full reflective design is completely diffraction limited. The spot diagrams are shown in Figure 12 below.

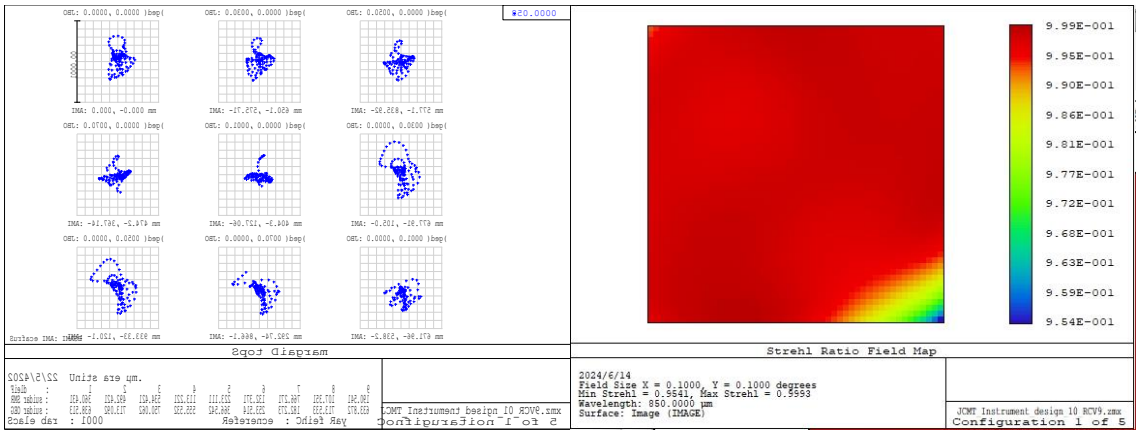

Figure 12. Spot diagrams and Strehl ratio map for the full reflective design (Design 5 in Figure 6). The spots are taken from the field center to the edge evenly sampled the 12 arcmin FoV diameter. The airy disc size is much larger than the spot sizes and not shown in this figure.

For the hybrid design, the purpose is to explore the possibilities other than the traditional mirror design. The hybrid design inside the receiver cabin remains the same with three mirrors to guide the light throughout the bearing tube. The out-of-cabin part adopts three lenses and one folding mirror. The space envelope for this hybrid design is roughly 2500mm × 900mm × 900mm, which is much smaller than the all-mirror design. The optical layout is shown in Figure 13 below.

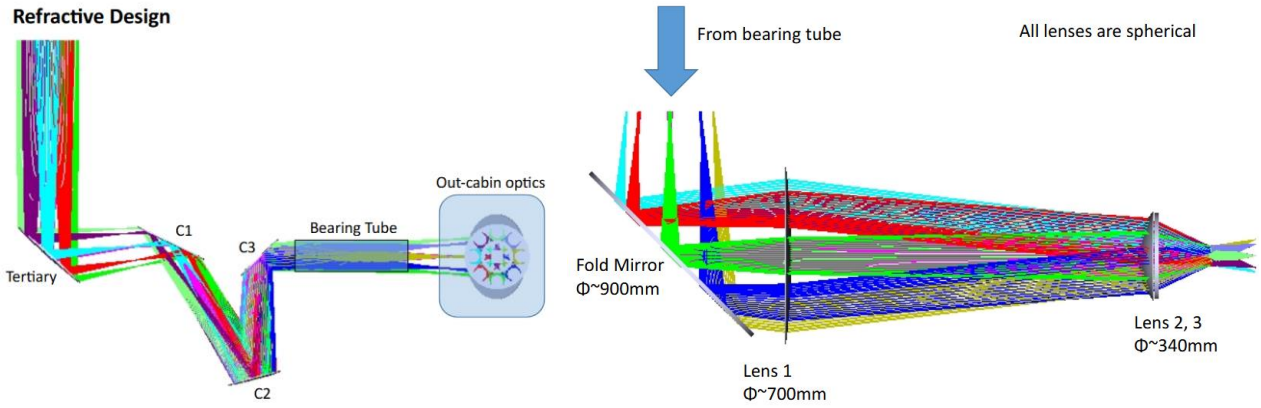

Figure 13. Left panel shows the overall layout of the hybrid design (Design 6 in Figure 6), the right panel shows the zoomed view of the part outside the receiver cabin.

The out-of-cabin part contains one fold mirror and three alumina lenses. All lenses have spherical surfaces. The largest lens has a diameter of about 700mm. The lens 1 size can be reduced by 40% if we take the folding mirror out. If necessary, the alumina lenses can be changed to silicon ones without changing too much parameters. The optical performance is close to the diffraction limited case. In general, the spot sizes throughout the field are smaller than the airy disc. The spot diagrams and Strehl ratio maps are shown in Figure 14.

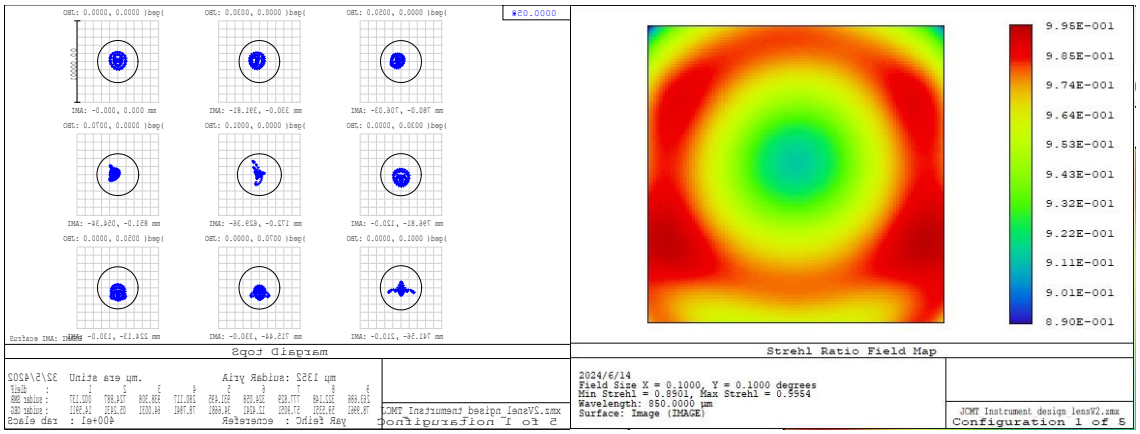

Figure 14. Spot diagrams and Strehl ratio map of the hybrid design (Design 6 in Figure 6). The dark circle represents the size of diffraction airy disc. The spots are taken from the same field positions shown in Figure 12.

4.4 Design comparisons

We compare the optical performance of the in-cabin and out-of-cabin design in terms of: 1) the system transmission of the relay optics, 2) the total wavefront error and Strehl ratio, and 3) the overall efficiency. In order to do that, we have made the following assumptions:

- Reflection loss for polished aluminum alloy mirror surface is assumed to be 1.5%.
- According to previously published literature, the loss tangent of high resistivity silicon is assumed to be 7×10^{-5} at low temperature of T<40K. With parylene C or thin etched silicon as anti-reflection coating, the transmission at the lens surface is assumed to be 98%.
- Fabrication error for each mirror surface is assumed to be 3 µm rms (similar to SCUBA-2 specifications).
- Fabrication error for each lens surface is also assumed to be 3 µm rms.

Based on above assumptions, we count the number of mirror and lens surfaces after the sub-reflector for each design, calculate the interface and bulk losses respectively, and then derive the system transmission. The results are summarized in Table 2. The system transmission of the out-of-cabin design (Design 4 in Table 2) is 4.4% lower than that of the in-cabin design (Design 1 in Table 2), as a result of a longer chain of ambient mirrors.

Table 2. Comparison of the system transmission for different optical designs, with reference to SCUBA-2 optics

Instrument	# of Mirror Surfaces	# of Lens Surfaces	Interface Loss	Bulk Loss	System Transmission
SCUBA-2	9	0	0.127	0	0.873
Design 1	2	2	0.068	0.04	0.895
Design 2	4	4	0.132	0.07	0.807
Design 3	4	4	0.132	0.07	0.807
Design 4	6	2	0.123	0.03	0.851
Design 5	10	0	0.140	0	0.860
Design 6	5	6	0.179	0.01	0.811

Ruling out design 2 and 3, we investigate the imaging performance by calculating the total wavefront errors for the remaining four designs. This includes the design wavefront error and wavefront errors caused by mirror and lens surface errors. Finally, we calculate the overall Strehl ratio according to the Ruze formula. The wavefront errors associated with the primary and secondary mirrors are excluded as we focus on the relay optics. The results are listed in Table 3. The overall Strehl ratio for the in-cabin design is 2.1% higher than that of the out-of-cabin design as a result of less design aberrations and fewer number of mirrors.

Table 3. Comparison of total wavefront error and overall Strehl ratio

	Design HWFE (μm rms)	RSS of mirror HWFEs (μm rms)	RSS of Lens HWFEs (μm rms)	RSS of all HWFEs (μm rms)	Overall Strehl Ratio
Design 1	10.7	4.2	5.0	12.5	0.966
Design 4	13.7	7.3	5.0	16.3	0.945
Design 5	2.1	9.5	0	9.7	0.979
Design 6	16.5	6.7	7.3	19.3	0.922

Finally, the overall performance comparison for the in-cabin and out-of-cabin designs is summarized in Table 4. Both designs deliver a FoV of 12 arcmin and an F/2.5 final planar and telecentric focal surface. The FoV is limited by the bearing tube for the out-of-cabin design and limited by the cabin pillars for the in-cabin design. We estimate the overall efficiency by multiplying the system transmission with overall Strehl ratio.

Table 4. Comparison of the overall performances

	FoV	Focal Ratio	System Transmission	Overall Strehl Ratio	Overall Efficiency
Design 1	Φ12’	F/2.5	0.895	0.966	0.865
Design 4	Φ12’	F/2.5	0.851	0.945	0.804
Design 5	12’ × 12’	F/2.4	0.860	0.979	0.842
Design 6	12’ × 12’	F/2.4	0.811	0.922	0.748

4.5 Summary

To get the best optical design possible and practical, we have developed a total of six: one in-cabin and five out-of-cabin, with following considerations: 1) Maximum achievable field of view; 2) The space confinement; 3) The offline time for SCUBA-2; 4) Impact of the antenna tilting, for the cryogenics and the polarimeter; 5) The modification to the current telescope structure needed; 6) The possibility of accommodating FTS-2.
We are currently at the milestone to choose between the in-cabin and out-of-cabin optical design. The cryogenics design and fabrication will then commence.

5. CRYOGENICS

We are aiming for a stable focal plane temperature below 100mk. As mentioned earlier, we still haven’t confirmed the optical design yet. The in- or out-of-cabin optics will dictate the cryogenic design. For now, we’ve investigated both possibilities and came up with a preliminary concept for them. Once the optical design is confirmed, the cryogenics and mechanical team will be involved.
For the in-cabin optics, constant tipping and moving during observations would pose a challenge to the performance of the cryogenic system. For now, a two stage Adiabatic Demagnetization Refrigerator (ADR) combined with a Pulse Tube closed cycle Cryocooler (PTC) would be the first choice. To minimize the effect of the antenna constantly tipping, the PTC cold head is designed to be vertical when the antenna is at about 50 degrees in elevation. Therefore, it would operate no more than 30 degrees from vertical when observing, as illustrated in the conceptual cryogenics design in Figure 15.

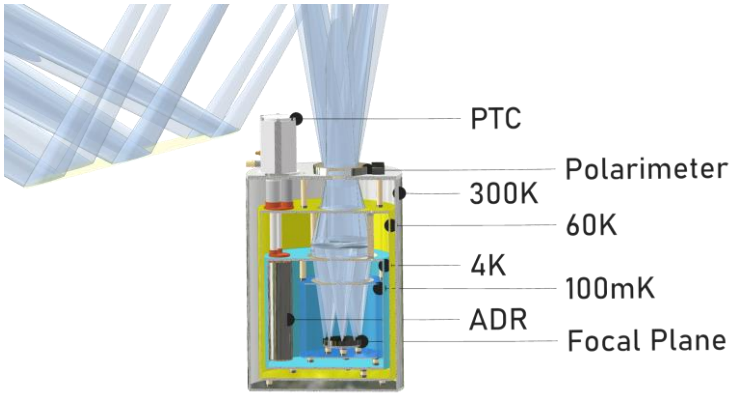

Figure 15. Conceptual cryogenics design for the in-cabin optics

If the new instrument is located outside the receiver cabin, with much more available space, the cryogenics would have more flexibility. For continuous operation, a Mini Dilution Refrigerator (MDR) backed by a continuous 3He/4He fridge and a PTC would work well. Alternatively, using ADR with 24 - 48 operational hours for each re-cycling as mentioned in the in-cabin design is also optional.

6. READOUT, DATA ACQUISITION AND REDUCTION

The ease of multiplexing readout and simpler array fabrication have been the advantage of MKIDs detectors over the TES as used in SCUBA-2. The MKIDs array readout based on Radio Frequency System-on-Chip (RF SoC) have seen stable development [15][16] [17] over the past few years, and it's being more widely adopted on telescopes operating at different wavelengths, both on the ground[18] and in space[19]. The new SCUBA instrument will also follow this path. Once the hardware readout strategy is confirmed, the firmware and software development becomes the next step for the successful delivery of the readout system. The planned readout firmware will provide the capability of automatic array tuning and for compensation and re-tuning, to deal with the varying sky background loading during real-time observations.

Following the signal flow, the MKIDs array data would then be acquired with the necessary environment and telescope tracking data, and reduced afterwards. The current data reduction software for SCUBA-2[20] is rather complex, and attempts to create models to correct for various instrumental and atmospheric effects on the data. This would be modified appropriately to adjust for the measured performance of the new array, the changed geometry of the detector arrays, readout scheme, array calibration and polarimetry, as well as potentially changed scan patterns.

7. CONCLUSION

The SCUBA-2 replacement project has come to the milestone of choosing between the in-cabin and out-of-cabin optical design, which dictates the cryogenics design. Once we've taken all the factors into consideration, with some experimental data to support the choice, the project will speed up. We're now confident that within the East Asian Observatory regional partners, the project will be executed efficiently. The planned on-sky time for the new instrument is in 2028.

REFERENCES

[1] Holland, W. S. *et al.* SCUBA-2: the 10 000 pixel bolometer camera on the James Clerk Maxwell Telescope. *Monthly Notices of the Royal Astronomical Society* **430**, 2513–2533 (2013).

[2] Friberg, P. *et al.* POL-2: a polarimeter for the James-Clerk-Maxwell telescope. in *Millimeter, Submillimeter, and Far-Infrared Detectors and Instrumentation for Astronomy VIII* vol. 9914 991403 (SPIE, 2016).

[3] Bintley, D. *et al.* Commissioning SCUBA-2 at JCMT and Optimising the Performance of the Superconducting TES Arrays. *J Low Temp Phys* **167**, 152–160 (2012).

[4] Day, P. K., LeDuc, H. G., Mazin, B. A., Vayonakis, A. & Zmuidzinas, J. A broadband superconducting detector suitable for use in large arrays. *Nature* **425**, 817–821 (2003).
[5] Griffin, M. J., Bock, J. J. & Gear, W. K. Relative performance of filled and feedhorn-coupled focal-plane architectures. *Appl. Opt., AO* **41**, 6543–6554 (2002).
[6] Austermann, J. E. *et al.* Millimeter-Wave Polarimeters Using Kinetic Inductance Detectors for TolTEC and Beyond. *J Low Temp Phys* **193**, 120–127 (2018).
[7] http://toltec.astro.umass.edu/
[8] Bintley, D., Dempsey, J. T., Friberg, P., Holland, W. S. & MacIntosh, M. J. An upgraded SCUBA-2 for JCMT. in *Millimeter, Submillimeter, and Far-Infrared Detectors and Instrumentation for Astronomy VIII* vol. 9914 119–131 (SPIE, 2016).
[9] Bintley, D. *et al.* SCUBA-2: an update on the performance of the 10,000 pixel bolometer camera after two years of science operation at the JCMT. in *Millimeter, Submillimeter, and Far-Infrared Detectors and Instrumentation for Astronomy VII* vol. 9153 42–56 (SPIE, 2014).
[10] https://github.com/TolTEC-Camera/MappingSpeedModel
[11] Bryan, S. *et al.* Optical design of the TolTEC millimeter-wave camera. in *Millimeter, Submillimeter, and Far-Infrared Detectors and Instrumentation for Astronomy IX* vol. 10708 143–150 (SPIE, 2018).
[12] Hill, C. A. *et al.* BoloCalc: a sensitivity calculator for the design of Simons Observatory. in *Millimeter, Submillimeter, and Far-Infrared Detectors and Instrumentation for Astronomy IX* vol. 10708 1016–1036 (SPIE, 2018).
[13] https://lweb.cfa.harvard.edu/~spaine/am/
[14] Brien, T. L. R. *et al.* MUSCAT: The Mexico-UK Sub-Millimetre Camera for AsTronomy. *Millimeter, Submillimeter, and Far-Infrared Detectors and Instrumentation for Astronomy IX* 20 (2018).
[15] McHugh, S. *et al.* A readout for large arrays of microwave kinetic inductance detectors. *Review of Scientific Instruments* **83**, 044702 (2012).
[16] Duan, R. & Golwala, S. Readout for kinetic-inductance-detector-based submillimeter radio astronomy. in *Millimeter, Submillimeter, and Far-Infrared Detectors and Instrumentation for Astronomy X* vol. 11453 252–285 (SPIE, 2020).
[17] Yan, X. *et al.* Readout System for Frequency-Division Multiplexing Superconducting Detector Arrays. *J Low Temp Phys* (2024)
[18] Bradley, D. C. *et al.* On the advancements of digital signal processing hardware and algorithms enabling the Origins Space Telescope. *JATIS* **7**, 011018 (2021).
[19] Sinclair, A. K. *et al.* CCAT-prime: RFSoC based readout for frequency multiplexed kinetic inductance detectors. in *Millimeter, Submillimeter, and Far-Infrared Detectors and Instrumentation for Astronomy XI* vol. 12190 444–463 (SPIE, 2022).
[20] Chapin, E. L. *et al.* SCUBA-2: iterative map-making with the Sub-Millimetre User Reduction Facility. *Mon Not R Astron Soc* **430**, 2545–2573 (2013).